This document is downloaded from DR-NTU (https://dr.ntu.edu.sg)
Nanyang Technological University, Singapore.

Improved photovoltaic performance of triple-cation mixed-halide perovskite solar cells with binary trivalent metals incorporated into the titanium dioxide electron transport layer

Thambidurai, Mariyappan; Foo, Shini; K. M. Muhammed Salim; Harikesh, Padinhare Cholakkal; Bruno, Annalisa; Nur Fadilah Jamaludin; Lie, Stener; Mathews, Nripan; Dang, Cuong

2019

Thambidurai, M., Foo, S., K. M. Muhammed Salim, Harikesh, P. C., Bruno, A., Nur Fadilah Jamaludin., ... Dang, C. (2019). Improved photovoltaic performance of triple-cation mixed-halide perovskite solar cells with binary trivalent metals incorporated into the titanium dioxide electron transport layer. Journal of Materials Chemistry C, 7(17), 5028-5036. doi:10.1039/c9tc00555b

https://hdl.handle.net/10356/143192

https://doi.org/10.1039/C9TC00555B

© 2019 The Royal Society of Chemistry. All rights reserved. This paper was published in Journal of Materials Chemistry C and is made available with permission of The Royal Society of Chemistry.

Downloaded on 28 Aug 2022 06:02:00 SGT

Improved photovoltaic performance of triple cation mixed-halide perovskite solar cells with binary trivalent metals incorporated on titanium dioxide electron transport layer

M. Thambidurai[1,2] , Foo Shini[1,2,3], K. M. Muhammed Salim[2], P. C. Harikesh[2], , Annalisa Bruno[2], Nur Fadilah Jamaludin[2], Stener Lie[2], Nripan Mathews[2,3], and Cuong Dang[1,2]*

1. LUMINOUS! Centre of Excellence for Semiconductor Lighting and Displays, School of Electrical and Electronic Engineering, The Photonics Institute (TPI), Nanyang Technological University, 50 Nanyang Avenue, 639798, Singapore.
2. Energy Research Institute @NTU (ERI@N), Research Techno Plaza, X-Frontier Block, Level 5, 50 Nanyang Drive, 637553, Singapore.
3. School of Materials Science and Engineering, Nanyang Technological University, 50 Nanyang Avenue, 639798, Singapore.

*Email: hcdang@ntu.edu.sg

Abstract

Perovskite solar cells have allured tremendous recognition and regards among the next-generation photovoltaic technologies. Besides the perovskite absorber component, adjacent layers within the stack also play decisive roles in the stability and overall power conversion efficiency (PCE) of the device. In this work, we demonstrated the use of solution-processed aluminium indium (AlIn)-TiO_2 compact layer as a highly effective electron transport layer (ETL) material for outstanding perovskite solar cells performance. Our results showed that the incorporation of AlIn into the TiO_2 layer allowed better energy band alignment of the ETL-perovskite interface, improved transparency, and enhanced conductivity compared to pristine TiO_2. Through the co-doping of these trivalent metals, enhancement in voltage, current density, and even fill factor were observed. In addition, results from electrochemical impedance spectroscopy (EIS) revealed that AlIn-TiO_2 based device exhibited larger recombination resistance, which tremendously benefited the performance of the devices. As such, the optimized AlIn-TiO_2 ETL device attained surpassing PCE of 19 % unlike the pristine TiO_2 solar device of 16.67 %.

Keywords: perovskite solar cells, AlIn-TiO_2, electron transport layer, time-resolved photoluminescence, electrochemical impedance spectroscopy.

1. Introduction

In recent years, organic-inorganic halide perovskite materials have been intensively studied owing to their potential applications in solar cells, light-emitting diodes, sensors, photodetectors, field effect transistors and lasers, etc.,.[1–6] Displaying excellent optical and electronic properties, perovskite materials are known for their high carrier mobility, tunable band gap, high absorption coefficient, low trap density, and great electron/hole diffusion length which are crucial for high performance photovoltaic devices.[7–11] In just a few years, tremendous increment in power conversion efficiency (PCE) was achieved from a humble 3.8% to 23.7%.[12–15] Generally, the conventional configuration of a perovskite solar cell includes an electron transporting layer (ETL), followed by the perovskite absorber layer and a hole transporting layer.[16] In perovskite solar cells, the ETLs play critical roles in both the collection and transportation of photogenerated electrons, as well as in the suppression of the electron-hole recombination. Theoretically, an ideal ETL should meet the following qualities: good optical transparency, high efficiency in transporting electrons and blocking holes, good electrical conductivity, and well-matched energy levels with perovskite materials.[17–19]

In pursuit for a highly effective ETL, various wide band gap semiconducting materials such as ZnO, SnO_2, and TiO_2 have been introduced in hopes of enhancing the overall photovoltaic performance. Amidst the various materials, titanium dioxide (TiO_2) emerged as a promising ETL candidate thanks to its good transparency, chemical inertness, air stability, low cost, and non-toxicity.[20,21] However, TiO_2 is an n-type semiconducting material with a wide band-gap of 3.2 eV. Compared to ZnO and SnO_2, TiO_2 ETLs have relatively low electron mobility and poor electrical conductivity. As a result, metal doping is commonly employed to improve the electrical properties of TiO_2 compact layer, as well as tailor the energy band structure for easy transportation of electrons from the perovskite layer to the transparent electrode.[22,26] Furthermore, several researchers had shown that the use of suitable n-type dopants into TiO_2 could alter the material properties of pure TiO_2 (grain size, orientation,

conductivity, and optical properties), such that the rate of recombination is reduced while the electron transport/injection properties are improved.[27,30] To illustrate, Zhang et al. reported that a solution-processed Mg-doped TiO_2 compact layer enhances the electron injection/ transport properties through the reduction in resistivity.[31] Li et al., on the other hand, fabricated perovskite solar cells using a spray-coated La-doped TiO_2 compact layer and achieved an efficiency of 17.2 %.[32] Similarly, Lv et al. showed the effective use of Zn-doped TiO_2 as an efficient ETL with the fabricated cell having relatively good efficiency of 15.25 % with enhanced device stability.[33] Aluminium has proven itself to be a promising dopant especially when used in the TiO_2 lattice. Apart from its relative abundance and low cost, the addition of aluminium has been reported to significantly improve the relatively poor conductivity of TiO_2.[34] When Ti^{4+} is replaced with a smaller oxidation state ion such as Al^{3+}, substitutional point defects such as oxygen vacancies are introduced. As such, the addition of aluminium should, theoretically, enhance the charge carrier concentration along with the electrical conductivity of the poorly conductive TiO_2 electron transporting film.[35] For example, Roose et al. reported that Al-doped TiO_2 films exhibited excellent optical transparency and low resistivity. [36] In good agreement, Yun et al. also reported the use of Al-doped TiO_2 based perovskite solar cells having efficiencies of 14.7 %. [30] On the other hand, the addition of indium metal is reported to reduce the work function of most oxide films due to the generation of large amount of free electrons.[37] In particular, Peng et al. showed improved band alignment between Indium doped TiO_2 compared to pristine TiO_2 ETL whereby the work function of In-TiO_2 is closer to the conduction band energy level of perovskite. [38] This being said, it is often hard to improve several cell parameters using simple ETL modification. For example, it is difficult to boost both fill factor (FF) through reduction in work function and/or enhanced conductivity whilst also improving the short-circuit current density (J_{sc}) via improved transparency of device. Therefore, there remain a large deficiency in the usage of simple ETL

modification to enhance several cell parameters such as improved FF, J_{sc}, and energy alignment, simultaneously.

In this paper, we added trivalent dopants of aluminium and indium into the conventional TiO_2 ETL layer to form AlIn-TiO_2 ETL via simple solution-based processing. By adding aluminium and indium at stoichiometric amounts into the conventional TiO_2 precursor solution, superior performance was achieved with the champion cell showing significantly higher PCE of 19 % compared to the pristine TiO_2 devices of 16.67 %. This is due to the enhanced transparency and conductivity when AlIn is added into TiO_2 ETL as seen in the improved J_{sc} and FF, respectively. Furthermore, AlIn-TiO_2 also showed higher V_{oc} compared to pristine devices due to the reduced work function and better energy level alignment. We further explored the usage of individual dopants and discovered that the addition of aluminium significantly alters the transparency and optical quality of the perovskite device through the improved J_{sc} values. On the other hand, the addition of indium was discovered to allow better energy level alignment and conductivity as demonstrated by the enhanced V_{oc} and FF. As such, our work demonstrates a simple yet versatile co-doping method to utilize the advantages of both dopants and improve several cell parameters at once, whereby the employment of AlIn-TiO_2 displayed an upward- shift in conduction level, improved light transmittance, and enhanced electrical conductivity.

2. Results and discussion

The structural properties of the films were first characterized. **Figure S1** shows the XRD patterns of the pristine TiO_2 and AlIn-TiO_2 films. The diffraction patterns indicate the adoption of anatase structure, corresponding to the (101) plane for both film samples. The intensity of diffraction peaks decreased after the incorporation of Al and In, implying a loss of crystallinity. No other impurity phase was detected, indicating the absence of secondary phases in the as-

prepared AlIn-TiO_2 films. This could be attributed to the small amount of doping concentration used and/or homogeneous distribution of Al and In in TiO_2.

To confirm the successful incorporation of Al and In into the TiO_2 structure, XPS was utilized to unravel the chemical makeup of the fabricated films. The XPS spectra of TiO_2 and AlIn-TiO_2 films are shown in **Figures 1(a-d)**. In good agreement with other studies, peaks were observed at binding energies of 458.25 and 464.06 eV representing the presence of Ti $2p_{3/2,}$ and Ti $2p_{1/2}$ in pristine TiO_2 films.[39] On the contrary, the Ti $2p_{3/2}$ and Ti $2p_{1/2}$ peaks found in the AlIn-doped TiO_2 film shifted by a small degree towards higher binding energies of 458.42 and 464.29 eV. Since Ti, Al, and In have electronegativity values of 1.54, 1.61, and 1.78 respectively, a negative charge transfer towards the smaller electronegativity aluminium and indium in the Ti-O-In-Al bond should occur.[38,40] As such, the shifting could be reasoned using the Pauling electronegativity theory by which a shift in Ti 2p core binding energy towards that of higher levels was observed. Furthermore, the peak for O 1s, as shown in **Figure 1b**, is found to be higher of 529.86 eV in AlIn-TiO_2 films compared to pristine TiO_2 film of 529.69 eV. In **Figure 1c**, In $3d_{5/2}$ and In $3d_{3/2}$ peaks are represented by the binding energies of 444.21 and 451.78 eV, respectively.[41] The binding energy of Al_{2p}, as shown in **Figure 1d**, is located at 74.19 eV.[42] In our AlIn-TiO_2 film, 0.01M of Al and 0.01M of In are added to the dopant precursor solution. According to the XPS results obtained for our AlIn-TiO_2 film, the atomic concentration of Ti, O, Al and In in the doped TiO2 films are 26.95 %, 70.98 %, 1.35 % and 0.72 %, respectively. In essence, the XPS results suggest successful incorporation of both aluminium and indium elements into the TiO_2 lattice.

Ultraviolet photoelectron spectroscopy (UPS) and UV-visible transmittance spectroscopy were utilized to examine the energy levels of TiO_2 and AlIn-TiO_2 films. As shown in **Figure 1e**, the valence band maximum (E_{VBM}) energy levels of TiO_2 and AlIn-TiO_2 films are -7.45 and -7.24 eV respectively, calculated from the equation $E_{VBM}=-[21.22-(E_{cutoff}-E_{onset})]$, where E_{cutoff} is the higher binding energy cutoff and E_{onset} is the onset energy in valence band

region. Furthermore, the conduction band minimum (E_{CBM}) energy levels were estimated using the corresponding optical band gap and E_{VBM} levels. As seen in **Figure S2**, AlIn-doped TiO_2 displays better optical transmittance compared to pristine TiO_2 ETL film at wavelengths between 400 to 900 nm. The higher transmittance consequently contributes towards the improved photocurrent. To calculate the band gap of the as-prepared films, we employed Tauc equation: $(\alpha h\upsilon) = A(h\upsilon - E_g)^{\frac{1}{2}}$ with α being the absorption coefficient, h as the Planck's constant, A as a constant, while E_g and υ representing the band gap and corresponding frequency of radiation. **Figure 1f** shows the plot of $(\alpha h\upsilon)^2$ against hυ for both TiO_2 and AlIn-TiO_2 films. Using the formula as mentioned above, the band gap of TiO_2 and AlIn- TiO_2 films were estimated by the extrapolation of a straight linear fit over the energy axis in the Tauc plots. The band gap of AlIn-TiO_2 films was found to be 3.31 eV, higher than that of TiO_2 film (3.20 eV). The calculated E_{CBM} levels of TiO_2 and AlIn-doped TiO_2 films were -4.25 and -3.93 eV, respectively.

Figure 2a shows the schematic representation of the fabricated perovskite device consisting of the following layers: FTO-coated glass substrate as the transparent electrode, TiO_2 or AlIn-TiO_2 as the ETL, meso-TiO_2, triple cation perovskite layer, hole transporting spiro-OMeTAD layer, and the gold (Au) layer as the back-contact. The exact cross-sectional morphology of the complete solar device is seen in **Figure 2b** with their equivalent thickness of compact AlIn-doped TiO_2, mesoporous TiO_2, perovskite, spiro-OMeTAD, and Au films to be 60, 200, 390, 180, and 80 nm, respectively. The energy level diagrams of the materials, inclusive of the characterized energy levels of TiO_2 and AlIn-TiO_2, are shown in **Figure 2c**. The valence band maximum (VBM) and conduction band minimum (CBM) values of meso-TiO_2 and perovskite were taken from literatures.[43,44] The highest occupied molecular orbital (HOMO) for the spiro-OMeTAD were reported as -5.20 eV while the lowest unoccupied molecular orbital (LUMO) was -2.50 eV.[45] Since the CBM level of AlIn-TiO_2 (-3.93 eV) is

closer to that of perovskite energy level compared to TiO_2 (-4.25 eV), transportation of electrons towards the FTO electrode should occur with less potential losses in AlIn-TiO_2 based devices. Moreover, the HOMO levels of both AlIn-TiO_2 (–7.24 eV) and TiO_2 (-7.45 eV) are much lower than that of perovskite (-5.40 eV) and spiro-OmeTAD (-5.20 eV), ensuring effective hole blocking whereby hole transport from spiro-OmeTAD to the Au electrode is carried out efficiently.

The TiO_2, Al-TiO_2, In-TiO_2, and AlIn-TiO_2 layers were deposited on the FTO substrates by spin coating. We had optimized the Al-TiO_2 and In-TiO_2 compact layers by using different precursor concentrations (0.02 M, 0.04 M, and 0.06 M) which were obtained using simple sol-gel method containing different amounts of aluminum nitrate nonahydrate and indium (III) nitrate hydrate added to a fixed volume of solvent of 2-methoxyethanol (5 mL) and acetylacetone (230 µL). The triple cation based perovskite devices with varied ETL materials namely TiO_2, Al-TiO_2, In-TiO_2, and AlIn-TiO_2 were fabricated and studied. As seen in **Figure 2d**, the current density–voltage (J–V) properties of TiO_2 and AlIn-TiO_2 based devices are examined. These measurements were carried out in ambient air under AM1.5G illumination at a light intensity of 100 mW cm^{-2}. The device performance given in **Table 1** shows a good contrast between devices fabricated with TiO_2 and AlIn-TiO_2 ETL. Displaying relatively poorer performance, the control device consisting of TiO_2 ETL achieved PCE of 16.67 %, open-circuit voltage (V_{oc}) of 1.04 V, short-circuit current density (J_{sc}) of 21.17 mA cm^{-2}, alongside with fill factor (FF) of 75.43 %. On the other hand, solar cell which used 0.02 M Al-TiO_2 ETL achieved a PCE of 17.98% with V_{oc}, J_{sc}, and FF corresponding to 1.05 V, 22.07 mA cm^{-2}, and 77.18 % respectively. Further addition of Al-doping, however, deteriorated the performances of the devices with corresponding PCE of 17.43 and 17.15 % for 0.04 M and 0.06 M Al-TiO_2 ETL based devices, respectively. Perovskite solar cells with 0.02 M In-TiO_2 exhibited PCE of 18.04 % with a V_{oc} of 1.05 V, J_{sc} of 21.75 mA cm^{-2}, and FF of 78.67 %. Varying the In-concentration of the In-TiO_2 based devices also resulted in a similar trend to that observed in

Al-doping. More details regarding the device performance with varying Al and In concentrations are summarized in **Table S1** and **Figure S3**. For the purpose of PCE enhancement, precursor concentration of 0.02 M was determined as the optimal concentration for superior device photovoltaic performance (V_{oc}, J_{sc} and FF) as seen in both Al-TiO_2 and In-TiO_2 ETL based cells, relative to the pristine TiO_2 ETL. When the device was co-doped with 0.01 M Al and 0.01 M In, the AlIn -TiO_2 ETL based devices delivered paramount performance with V_{oc} of 1.07 V, J_{sc} of 22.30 mA cm^{-2}, FF of 79.50 %, and overall device efficiency of 19 %. To further improve the optical transmittance and device performance, anti-reflection film was attached to the front side of the glass substrate. As seen in **Figure S4**, AlIn-TiO_2 based device with anti-reflection film exhibited PCE of 19.31 % with a V_{oc} of 1.07 V, J_{sc} of 22.66 mA cm^{-2}, and FF of 79.60 %.

AlIn-TiO_2 ETL has higher optical transmission **(Figure S2)** and wider energy band gap **(Figure 1f)**, accounting to the higher J_{sc} values observed in the AlIn-TiO_2 based solar cells. The series resistance (R_{series}) and shunt resistance (R_{shunt}) were derived from J-V curves. It is notable that the AlIn-TiO_2 based device has smaller R_{series} and larger R_{shunt} than the pristine TiO_2 device. As such, a higher FF was observed. Furthermore, the conductivity, Hall mobility, and carrier density were also measured using the Hall effect measurements. As shown in **Table S2**, the conductivity of AlIn-doped TiO_2 is higher than that of pristine TiO_2 films. This could be caused by the increased Hall mobility and carrier density, thus reducing the series resistance in AlIn-TiO_2 based device.

Steady state efficiencies were also studied on both TiO_2 and AlIn-TiO_2 based devices. As seen in **Figure 2e**, the perovskite solar cells with AlIn-TiO_2 ETL display J_{sc} of 20.04 mA cm^{-2} and PCE of 18.06 % at voltage bias of 0.90 V. On the contrary, perovskite solar cells with TiO_2 ETL demonstrated poorer J_{sc} of 18.64 mA cm^{-2} and PCE of 15.60 % at voltage bias of 0.83 V. The incident photon-to-current conversion efficiency (IPCE) spectra of TiO_2, Al-TiO_2, In-TiO_2, and AlIn-TiO_2 based perovskite solar cells are shown in **Figure 2f** and **S5**. It can be

seen that AlIn-TiO_2 based device exhibited higher IPCE intensity over the entire wavelength range from 300 to 780 nm when compared to the pristine TiO_2, Al-TiO_2, and In-TiO_2 based devices. The current density (J_{sc}) values of 19.54, 20.13, 19.94, and 20.58 mA cm^{-2} were achieved for TiO_2, Al-TiO_2, In-TiO_2, and AlIn-TiO_2 based devices, respectively. To check the reproducibility of the devices, we fabricated TiO_2 and AlIn-TiO_2 based devices as represented by **Figure 3**. Since the photovoltaic performance of each device only suffers small deviation, the as-fabricated devices display good reproducibility with the average PCE of TiO_2 and AlIn-TiO_2 based devices being 16.0 % and 18.20 %, respectively. In addition, we also examined the long-term stability of all the devices made without any encapsulation as seen in **Figure S6**. For pristine TiO_2 based device, retainment of initial PCE was approximately 80 % with corresponding V_{oc} of 1.04 V, J_{sc} of 19.85 mA cm^{-2}, FF of 65.26, and PCE of 13.47 %. On the contrary, AlIn-TiO_2 based device was able to retain 89 % of initial PCE with corresponding V_{oc} of 1.09 V, J_{sc} of 20.87 mA cm^{-2}, FF of 74.27, and PCE of 16.90 % even after storing the device for 25 days under ambient conditions. There are various reasons that affect the stability of perovskite solar cells such as interfacial defects on the surface, grain boundaries, deep trap assisted recombination. In our devices, the electrochemical impedance spectroscopy (EIS) data, as shown in the later part of this study (**Figure 5**), shows higher recombination resistance in the devices with AlIn-TiO_2. This implies that the devices with AlIn-TiO_2 layer possess significantly lower amount of traps compared to that with the pristine TiO_2 layer. As such, we postulate that one possible factor for the better stability could be due to the reduced amount of traps in the AlIn-TiO_2 layer, which further facilitates better charge transfer between ETL and perovskite.

We further investigated the optical behaviour of perovskite on the ETLs. The absorption spectra of perovskite on glass, perovskite on TiO_2, perovskite on AlIn-TiO_2 samples are shown in **Figure S7**. A slight blue shift of the perovskite films on TiO_2 and AlIn-doped TiO_2 films was observed when compared to pure perovskite film on glass. To investigate the charge recombination behaviour, the photoluminescence (PL) spectra of these samples were measured

using excitation at 600 nm as shown in **Figure 4a**. The peak observed at approximately 775 nm corresponds to the excited states (bound excitons) in the perovskite. When the perovskite layer was deposited on glass substrate, a sharp PL peak with high intensity was observed suggesting excellent quality of the fabricated perovskite film. Such high quality perovskite film allows bound excitons to exist for a long period of time in the film before having to separate into their individual electron and hole charge carriers. On the other hand, the PL intensity was found to be appreciably reduced when the perovskite film was deposited on top of the TiO_2 film. Even larger reduction was observed for the AlIn-TiO_2 film. A similar quenching trend was observed for the PL decay lifetimes as seen in **Figure 4b**. According to the time-resolved photoluminescence (TRPL) results, perovskite deposited on glass exhibited the longest average fluorescence lifetime ($\tau = 233.9$ ns). When perovskite is deposited on the TiO_2 film, a significant reduction in lifetime was recorded ($\tau = 208.5$ ns). Further reduction in lifetime was observed for the perovskite film deposited on AlIn-TiO_2 ($\tau = 150.1$ ns). Through the larger PL quenching observed in the AlIn-TiO_2 based film compared to pristine TiO_2, it is evident that co-doping of Al and In into TiO_2 allows superior charge separation of exciton formed in the perovskite layer. The full data is summarised in **Table S3**.

Electrochemical impedance spectroscopy (EIS) measurements were used to investigate the charge transport process, contact resistance, and carrier recombination of the TiO_2 and AlIn-TiO_2 based perovskite solar cells. Under dark condition, the Nyquist plots of TiO_2 and AlIn-TiO_2 based devices were recorded with an applied forward bias of 800 mV as shown in **Figure 5**. Generally, there are two arcs in the Nyquist plot; the first arc located in the high frequency region is related to the contact resistance of the interface, while the second arc located at lower frequencies corresponds to the recombination resistance and chemical capacitance of a device. An equivalent circuit **(Figure S8)** was used to fit the data in the Nyquist plots and the corresponding values representing the recombination (R_{rec}) and series (R_{series}) resistances are shown in **Table S4.**[46] As seen, the recombination resistance values of TiO_2 and AlIn-TiO_2

samples are 5.40 and 56.9 KΩ, respectively. Through the larger recombination resistance displayed in AlIn-doped TiO_2 sample and smaller recombination rate, it is evident that charge transport of carriers is greatly promoted using the co-doped ETL, accounting for the marked increase in J_{sc} compared to the pristine TiO_2 sample. As such, the superior V_{oc} and J_{sc} exhibited in the AlIn-doped TiO_2 device can be correlated to the highly efficient electron extraction/ transportation and lowered recombination rate.

3. Conclusion

In summary, our research demonstrates an effective method to boost several cell parameters via simple ETL modification. The addition of both trivalent Al and In into TiO_2 is believed to significantly enhance the overall photovoltaic efficiency via three factors. Firstly, the conductivity of AlIn-TiO_2 devices was tremendously improved as seen from the increased FF. Secondly, better band alignment in the modified ETL layer was observed whereby an upward shift in conduction band, reduced work function, and therefore, enhanced V_{oc} were observed compared to the pristine TiO_2 device. Finally, AlIn-TiO_2 devices also displayed an enhanced optical quality and transmittance as seen in the improved J_{sc} value. Through these simultaneous improvements in various photovoltaic cell parameters, paramount efficiency of 19% was attained via the usage of simple co-doping into conventional TiO_2 ETL.

4. Experimental Section

Materials: Titanium (IV) butoxide, aluminum nitrate nonahydrate, indium (III) nitrate hydrate, 2-methoxyethanol, acetylacetone, cesium iodide (CsI), ethanol, N,N-dimethylformamide (DMF), dimethyl sulfoxide (DMSO), spiro-OMeTAD, bis(trifluoromethylsulfonyl)amine lithium salt, 4-tert-butylpyridine, acetonitrile, and chlorobenzene were purchased from Sigma Aldrich. Lead (II) iodide (PbI_2), and lead (II) bromide ($PbBr_2$) were purchased from Tokyo

Chemical Industry (TCI). Formamidinium iodide (FAI), methylammonium bromide (MABr), and TiO_2 paste (30NRD) were purchased from Dyesol.

Preparation of AlIn-doped TiO_2 compact layer: In our study, AlIn-doped TiO_2 compact layer was prepared using simple sol-gel method with stoichiometric amounts of titanium (IV) butoxide (0.45 M), aluminum nitrate nonahydrate (0.01 M), and indium (III) nitrate hydrate (0.01 M) dissolved in 2-methoxyethanol and acetylacetone. After 3h stirring at room temperature, a clear and homogeneous light-yellowish solution was attained. To prepare thin films of AlIn-doped TiO_2 ETL, the as-prepared sol was spin coated onto the FTO surface. AlIn-doped TiO_2 thin films were formed after annealing at 500 °C for 1h.

Device fabrication: For perovskite solar cell fabrication, we followed a standard device configuration of FTO/AlIn-TiO_2/meso-TiO_2/perovskite/spiro-OMeTAD/Au. The fluorine-doped tin oxide (FTO) glass substrates were patterned using Zn powder and diluted HCl. The etched FTO glass substrates were sequentially cleaned through sonication in detergent, deionized water, and a variety of alcohols, followed by UV treatment for 20 min. AlIn-TiO_2 compact layer was then deposited on the FTO surface at a spin rate of 3000 rpm (at an acceleration of 500 rpm) for 40 s. Later, the coated FTO substrates were annealed at 500 °C for 1h in air and cooled to room temperature. Mesoporous TiO_2 (meso-TiO_2) was prepared by dissolving TiO_2 (30-NRD) paste in absolute ethanol. The as-prepared meso-TiO_2 solution was then spun at 5000 rpm for 30 s and annealed at 500 ºC for 15 min. Subsequently, the samples were subjected to UV ozone treatment before the perovskite spin coating. To prepare the perovskite precursor solution, 507 mg of PbI_2 (1.1 M), 172 mg of FAI (1.0 M), 81 mg of $PbBr_2$ (0.22 M), 22.3 mg of MABr (0.2 M) were added to 1 mL of mixture consisting of 800 µL of anhydrous DMF with 200 µL of anhydrous DMSO. Then, 42 µL of the stock solution of CsI (1.5 M) was added to the above-mentioned mixed solution. The solution was stirred for 3 h at room temperature. The triple cation perovskite solution was deposited through a two-step spin coating program; first at 2000 rpm for 10 s and then at 6000 rpm for 30 s. 15s into the second

step, 100 µL of chlorobenzene was drop casted onto the spinning substrate followed by an hour of annealing at 100 ºC. Dissolved in 1 mL of chlorobenzene, 70 mg spiro-OmeTAD, 28 µL 4-tert-butylpyridine, 16.94 µL bis(trifluoromethylsulfonyl)amine lithium salt, and 35 µL FK209 Co(III) TFSI salt (18.8 mg/50 µL in acetonitrile) were used to prepare the spiro-OMeTAD solution. Afterwards, the solution was spun at 4000 rpm for 30 s to form a thin Spiro-OMeTAD above the perovskite layer. The perovskite and spiro-OMeTAD depositions were carried out in an argon filled glove box. Finally, thermal evaporation was employed to deposit 80 nm of gold as the last layer of the complete device.

Characterization*:* X-ray diffraction (XRD) studies were carried out using a x-ray diffractometer (D8 Advance). Photoelectron spectrometer (AXIS-His) was utilized for X-ray photoelectron spectroscopy (XPS, AXIS-HSi). Ultraviolet photoelectron spectroscopy (UPS) measurements utilized AXIS Ultra DLD (KRATOS Inc.) consisting of a monochromatic He I (21.22 eV) light source. Morphologies of devices were examined using field emission scanning electron microscope (JEJOL JSM-7600F). For current density-voltage (J-V) characterisation, the Keithley 2612A source meter unit was used under simulated Air Mass 1.5 global (AM 1.5G) solar illumination with an intensity of 100 mW/cm^2. The light intensity of solar simulator was calibrated against a standard silicon device. Incident photon-to-current conversion (IPCE) spectra were obtained using the dual xenon/quartz halogen light PVE300 (Bentham) source without light bias. Absorption spectra were measured by the UV-vis spectrophotometer (Shimadzu, UV-1800). Photoluminescence (PL) spectra of the films were recorded using a spectrofluorophotometer (Shimadzu, RF-5301PC). The effective area of the solar cell was 0.090 cm^2. Electrical properties of films were determined by Hall Effect measurements (MMR Technologies, H-50) using Van der Pauw method. Time-resolved photoluminescence (TRPL) measurements were conducted using a time-correlated single photon counting (TCSPC) system (PicoQuant, PicoHarp 300). A picosecond-pulsed laser diode (λ = 405 nm, f = 40 MHz) (Picoquant P-C-405B) was used to excite the sample. Impedance spectroscopy was measured

inside an argon filled glove box with an Autolab PGSTAT302N by applying a 20 mV perturbation with frequencies varying from 10 Hz to 1 MHz at a DC voltage of 800 mV under dark condition.

Acknowledgements

We would like to thank the financial support from Singapore Ministry of Education through AcRF Tier1 grant MOE2017-T1-002-142. We would thank Prof. Subodh Mhaisalkar, Executive Director of Energy Research Institute @ NTU (ERI@N) for supporting this work. The authors acknowledge Facility for Analysis, Characterization, Testing and Simulation (FACTS), Nanyang Technological University, Singapore, for the use of XPS/UPS facilities.

References

[1] X. Y. Chin, D. Cortecchia, J. Yin, A. Bruno, C. Soci, *Nat. Commun.* **2015**, *6*, 7383.

[2] Y. F. Ng, S. A. Kulkarni, S. Parida, N. F. Jamaludin, N. Yantara, A. Bruno, C. Soci, S. Mhaisalkar, N. Mathews, *Chem. Commun.* **2017**, *53*, 12004.

[3] G. Kakavelakis, E. Gagaoudakis, K. Petridis, V. Petromichelaki, V. Binas, G. Kiriakidis, E. Kymakis, *ACS Sensors* **2018**, *3*, 135.

[4] H. Wang, D. H. Kim, *Chem. Soc. Rev.* **2017**, *46*, 5204.

[5] G. Xing, N. Mathews, S. S. Lim, N. Yantara, X. Liu, D. Sabba, M. Grätzel, S. Mhaisalkar, T. C. Sum, *Nat. Mater.* **2014**, *13*, 476.

[6] W. Chen, Y. Wu, Y. Yue, J. Liu, W. Zhang, X. Yang, H. Chen, E. Bi, I. Ashraful, M. Grätzel, L. Han, *Science* **2015**, *350*, 944.

[7] G. Xing, N. Mathews, S. Sun, S. S. Lim, Y. M. Lam, M. Grätzel, S. Mhaisalkar, T. C. Sum, *Science* **2013**, *342*, 344.

[8] S. De Wolf, J. Holovsky, S. J. Moon, P. Löper, B. Niesen, M. Ledinsky, F. J. Haug, J. H. Yum, C. Ballif, *J. Phys. Chem. Lett.* **2014**, *5*, 1035.

[9] G. E. Eperon, S. D. Stranks, C. Menelaou, M. B. Johnston, L. M. Herz, H. J. Snaith, *Energy Environ. Sci.* **2014**, *7*, 982.

[10] C. Wehrenfennig, G. E. Eperon, M. B. Johnston, H. J. Snaith, L. M. Herz, *Adv. Mater.* **2014**, *26*, 1584.

[11] S. D. Stranks, G. E. Eperon, G. Grancini, C. Menelaou, M. J. P. Alcocer, T. Leijtens, L. M. Herz, A. Petrozza, H. J. Snaith, *Science* **2013**, *342*, 341.

[12] A. Kojima, K. Teshima, Y. Shirai, T. Miyasaka, *J. Am. Chem. Soc.* **2009**, *131*, 6050.

[13] S. Sik Shin, E. Joo Yeom, W. Seok Yang, S. Hur, M. Gyu Kim, J. Im, J. Seo, J. Hong Noh, S. Il Seok, *Science* **2017**, *356*, 167.

[14] W. S. Yang, J. H. Noh, N. J. Jeon, Y. C. Kim, S. Ryu, J. Seo, S. Il Seok, *Science* **2015**, *348*, 1234.

[15] M. Saliba, T. Matsui, J. Y. Seo, K. Domanski, J. P. Correa-Baena, M. K. Nazeeruddin, S. M. Zakeeruddin, W. Tress, A. Abate, A. Hagfeldt, M. Grätzel, *Energy Environ. Sci.* **2016**, *9*, 1989.

[16] S. Shukla, S. Shukla, L. J. Haur, S. S. H. Dintakurti, G. Han, A. Priyadarshi, T. Baikie, S. G. Mhaisalkar, N. Mathews, *ChemSusChem* **2017**, *10*, 3804.

[17] J. W. Jung, C. C. Chueh, A. K. Y. Jen, *Adv. Mater.* **2015**, *27*, 7874.

[18] Y. Xiang, Z. Ma, J. Zhuang, H. Lu, C. Jia, J. Luo, H. Li, X. Cheng, *J. Phys. Chem. C* **2017**, *121*, 20150.

[19] A. Bruno, D. Cortecchia, X. Y. Chin, K. Fu, P. P. Boix, S. Mhaisalkar, C. Soci, *Adv. Energy Mater.* **2017**, *7*, 1.

[20] F. Giordano, A. Abate, J. P. Correa Baena, M. Saliba, T. Matsui, S. H. Im, S. M. Zakeeruddin, M. K. Nazeeruddin, A. Hagfeldt, M. Graetzel, *Nat. Commun.* **2016**, *7*.

[21] X. Chen, S. S. Mao, *Chem. Rev.* **2007**, *107*, 2891.

[22] H. Wang, R. Jiang, M. Sun, X. Yin, Y. Guo, M. He and L. Wang, *J. Mater. Chem. C*, 2019, **7**, 1948–1954.

[23] X. Yin, Z. Xu, Y. Guo, P. Xu and M. He, *ACS Appl. Mater. Interfaces*, 2016, **8**, 29580−29587.

[24] X. Yin, Y. Guo, Z. Xue, P. Xu, M. He and B. Liu, *Nano Res.*, 2015, **8**, 1997–2003.

[25] Z. Xu, X. Yin, Y. Guo, Y. Pu and M. He, *J. Mater. Chem. C*, 2018, **6**, 4746–4752.

[26] H. Wang, X. Yin and L. Wang, *J. Mater. Chem. C,* 2018, **6**, 11569–11574.

[27] X. Gu, Y. Wang, T. Zhang, D. Liu, R. Zhang, P. Zhang, J. Wu, Z. D. Chen, S. Li, *J. Mater. Chem. C* **2017**, *5*, 10754.

[28] Z. Zhang, J. Li, X. Wang, J. Qin, W. Shi, Y. Liu, H. Gao, Y. Mao, *RSC Adv.* **2017**, *7*, 13325.

[29] X. X. Gao, Q. Q. Ge, D. J. Xue, J. Ding, J. Y. Ma, Y. X. Chen, B. Zhang, Y. Feng, L. J. Wan, J. S. Hu, *Nanoscale* **2016**, *8*, 16881.

[30] J. Yun, J. Ryu, J. Lee, H. Yu, J. Jang, *J. Mater. Chem. A* **2015**, *4*, 1306.

[31] H. Zhang, J. Shi, X. Xu, L. Zhu, Y. Luo, D. Li, Q. Meng, *J. Mater. Chem. A* **2016**, *4*, 15383.

[32] H. Li, B. Zheng, Y. Xue, S. Liu, C. Gao, X. Liu, *Sol. Energy Mater. Sol. Cells* **2017**, *168*, 85.

[33] M. Lv, W. Lv, X. Fang, P. Sun, B. Lin, S. Zhang, X. Xu, J. Ding, N. Yuan, *RSC Adv.* **2016**, *6*, 35044.

[34] C. O'Rourke, D. R. Bowler, *J. Phys. Chem. C* **2014**, *118*, 7261.

[35] N. D. M. Said, M. Z. Sahdan, A. Ahmad, I. Senain, A. S. Bakri, S. A. Abdullah, M. S. Rahim, *AIP Conf. Proc.* **2017**, *1788*, 30130.

[36] B. Roose, S. Pathak, U. Steiner, *Chem. Soc. Rev.* **2015**, *44*, 8326.

[37] X. Liang, Y. Ren, S. Bai, N. Zhang, X. Dai, X. Wang, H. He, C. Jin, Z. Ye, Q. Chen, L. Chen, J. Wang, Y. Jin, *Chem. Mater.* **2014**, *26*, 5169.

[38] J. Peng, T. Duong, X. Zhou, H. Shen, Y. Wu, H. K. Mulmudi, Y. Wan, D. Zhong, J. Li, T. Tsuzuki, K. J. Weber, K. R. Catchpole, T. P. White, *Adv. Energy Mater.* **2017**, *7*.

[39] Q. Cai, Y. Zhang, C. Liang, P. Li, H. Gu, X. Liu, J. Wang, Z. Shentu, J. Fan, G. Shao, *Electrochim. Acta* **2018**, *261*, 227.

[40] B. M. Reddy, B. Chowdhury, P. G. Smirniotis, *Applied Catalysis A: General* **2001**, *219*, 53.

[41] S. Coman, P. Grange, G. Poncelet, *Journal of Catalysis* **1998**, *180*, 66.

[42] G. Mohan Kumar, P. Ilanchezhiyan, A. Madhan Kumar, S. U. Yuldashev, T. W. Kang, *Chem. Phys. Lett.* **2016**, *649*, 130.

[43] M. Deepa, M. Salado, L. Calio, S. Kazim, S. M. Shivaprasad, S. Ahmad, *Phys. Chem. Chem. Phys.* **2017**, *19*, 4069.

[44] M. Thambidurai, H. A. Dewi, P. C. Harikesh, F. Shini, K. M. Muhammed Salim, N. Mathews, C. Dang, *ACS Appl. Energy Mater.* **2018**, *1*, 5847.

[45] J. Song, E. Zheng, L. Liu, X. F. Wang, G. Chen, W. Tian, T. Miyasaka, *ChemSusChem* **2016**, *9*, 2640.

[46] A. Guerrero, G. Garcia-Belmonte, I. Mora-Sero, J. Bisquert, Y. S. Kang, T. J. Jacobsson, J. P. Correa-Baena, A. Hagfeldt, *J. Phys. Chem. C* **2016**, *120*, 8023.

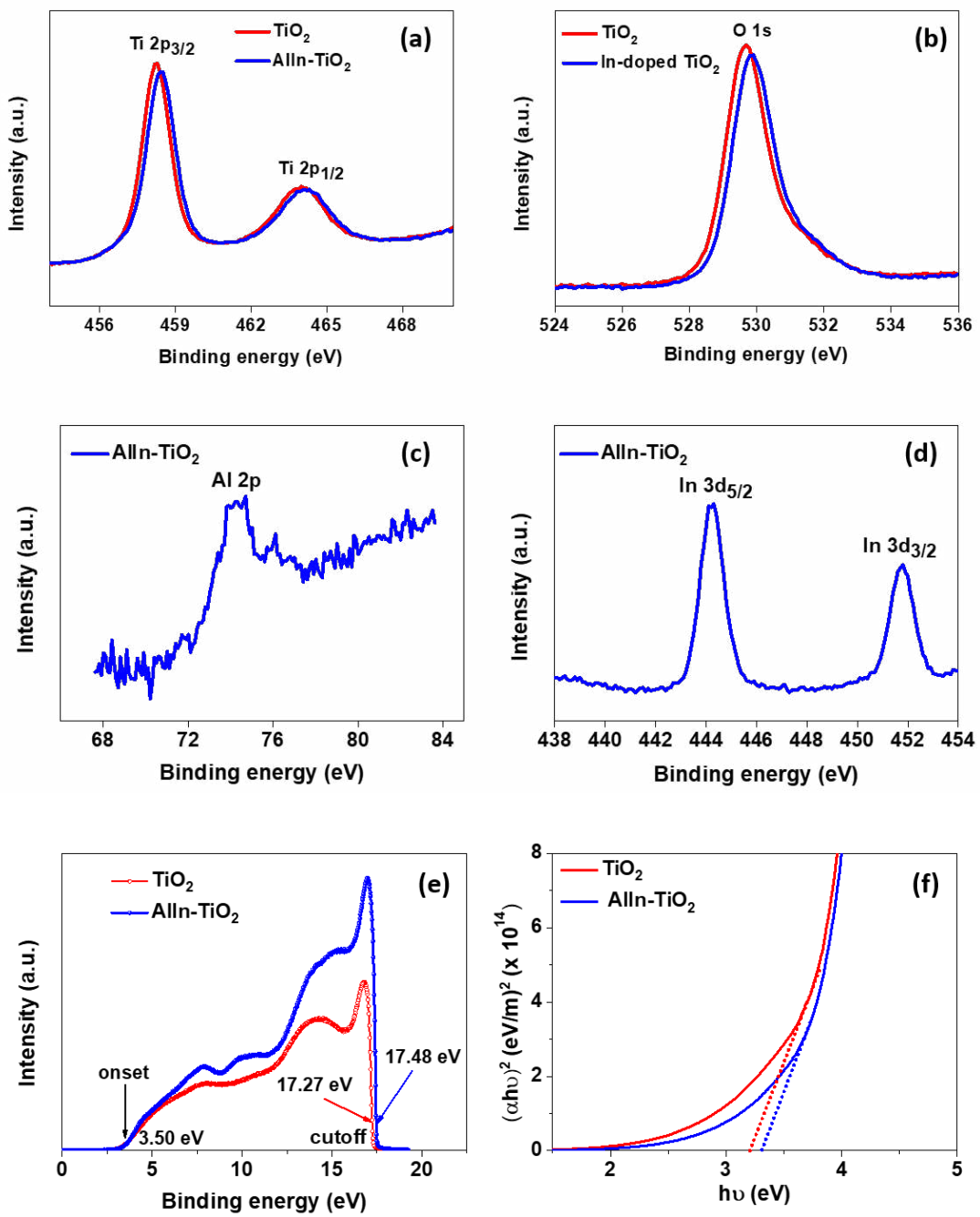

Figure 1. XPS spectra of TiO_2 and AlIn-TiO_2 films at the peaks of (a) Ti 2p, (b) O 1s, (c) Al 2p and (d) In 3d. (e) UPS spectra of TiO_2 and AlIn-doped TiO_2 films. (f) Plot of $(\alpha h\upsilon)^2$ versus $h\upsilon$ of TiO_2 and AlIn-TiO_2 films.

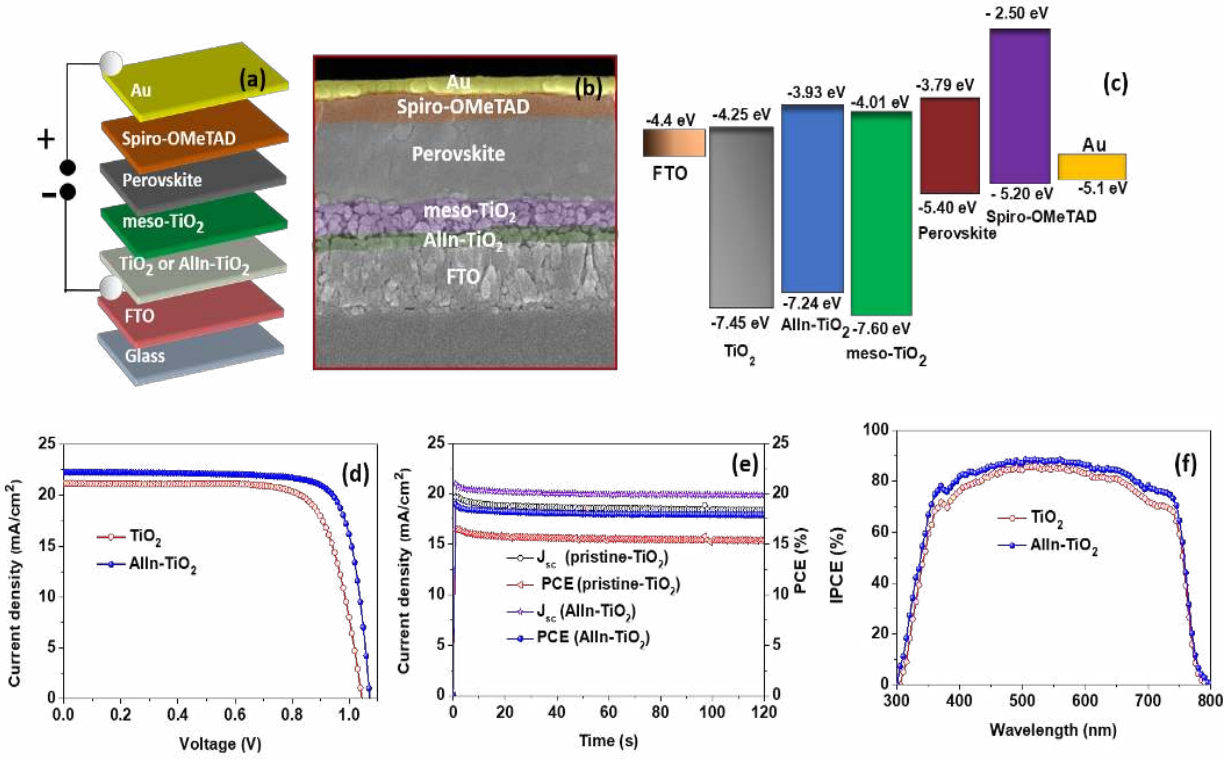

Figure 2. (a) The schematic structure of the perovskite solar cell device. (b) Cross-sectional SEM image of the device: Glass/FTO/AlIn-TiO_2/meso-TiO_2/perovskite/spiro-OMeTAD/Au. (c) Energy level diagram of the component materials used in device fabrication. (d) Current density-voltage (J-V) curves of the TiO_2 and AlIn-TiO_2 based perovskite solar cells. (e) The steady state efficiency of the pristine TiO_2 and AlIn-TiO_2 based perovskite devices measured at maximum power output. (f) Incident photon-to-current conversion efficiency (IPCE) of perovskite solar cells with TiO_2 and AlIn-doped TiO_2.

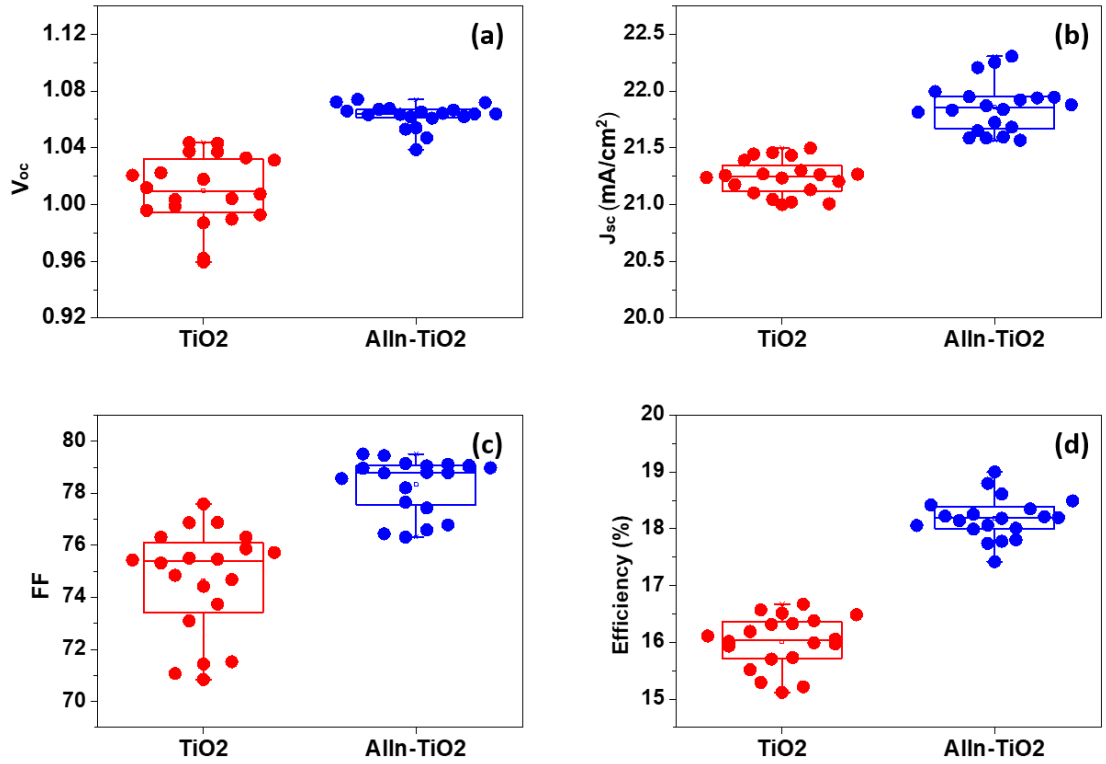

Figure 3. Statistical distribution of the photovoltaic parameters for solar cells with TiO_2 and AlIn-TiO_2: (a) distribution of V_{oc}, (b) distribution of J_{sc}, (c) distribution of FF, and (d) distribution of PCE.

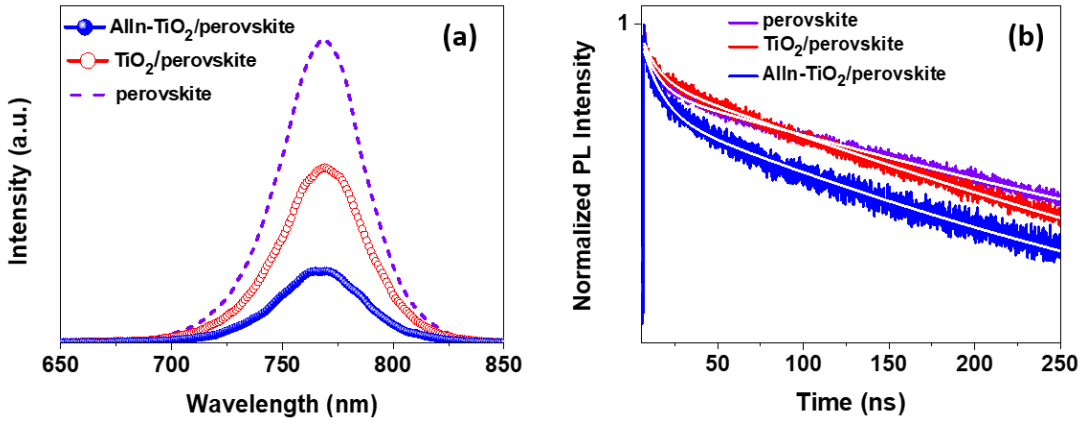

Figure 4. (a) Photoluminescence spectra of perovskite coated TiO_2 and AlIn-TiO_2 films. (b) TRPL spectra of perovskite absorber layer deposited on TiO_2 and AlIn-TiO_2. The data were fitted by a bi-exponential decay rate model (white colour).

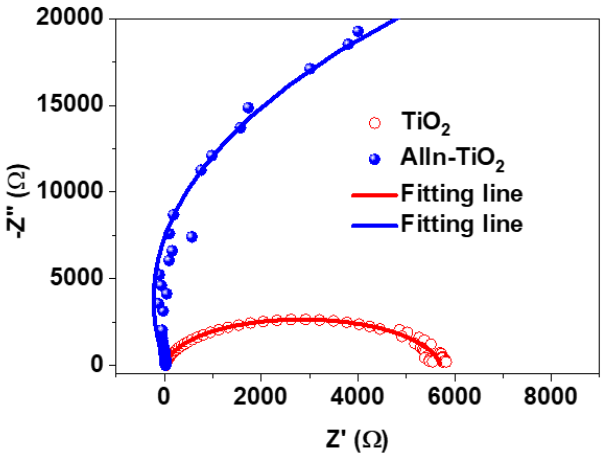

Figure 5. Nyquist plots of TiO_2 and AlIn-TiO_2 ETL based perovskite solar cells.

Table 1: Photovoltaic parameters of perovskite solar cells with pristine TiO_2, Al-TiO_2, In-TiO_2 and AlIn-TiO_2.

ETLs	V_{oc} [V]	J_{sc} [mA cm^{-2}]	FF [%]	PCE [%]	J_{sc} from IPCE [mA cm^{-2}]
TiO_2	1.04	21.17	75.43	16.67	19.54
0.02 M Al-doped TiO_2	1.05	22.07	77.18	17.98	20.13
0.02 M In-doped TiO_2	1.05	21.75	78.67	18.04	19.94
AlIn-TiO_2	1.07	22.30	79.50	19.00	20.58
AlIn-TiO_2 with anti-reflection coating	1.07	22.66	79.60	19.31	-

TOC:

Simultaneous improvement in transparency, conductivity, and energy level alignment were attained via a highly efficient AlIn-TiO_2 ETL with unrivaled PCE of 19%.

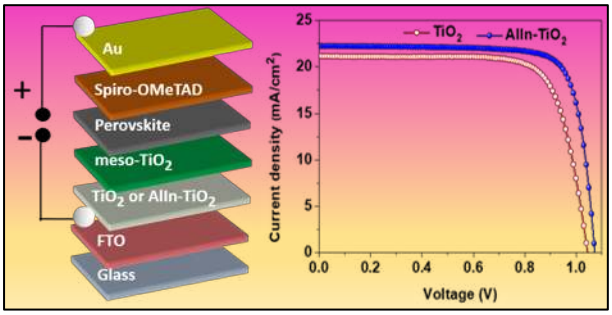

Supplementary Information

Improved photovoltaic performance of triple cation mixed-halide perovskite solar cells with binary trivalent metals incorporated on titanium dioxide electron transport layer

M. Thambidurai[1,2] , Foo Shini[1,2,3], K. M. Muhammed Salim[2], P. C. Harikesh[2], , Annalisa Bruno[2], Nur Fadilah Jamaludin[2], Stener Lie[2], Nripan Mathews[2,3], and Cuong Dang[1,2]*

1. LUMINOUS! Centre of Excellence for Semiconductor Lighting and Displays, School of Electrical and Electronic Engineering, The Photonics Institute (TPI), Nanyang Technological University, 50 Nanyang Avenue, 639798, Singapore.
2. Energy Research Institute @NTU (ERI@N), Research Techno Plaza, X-Frontier Block, Level 5, 50 Nanyang Drive, 637553, Singapore.
3. School of Materials Science and Engineering, Nanyang Technological University, 50 Nanyang Avenue, 639798, Singapore.

*Email: hcdang@ntu.edu.sg

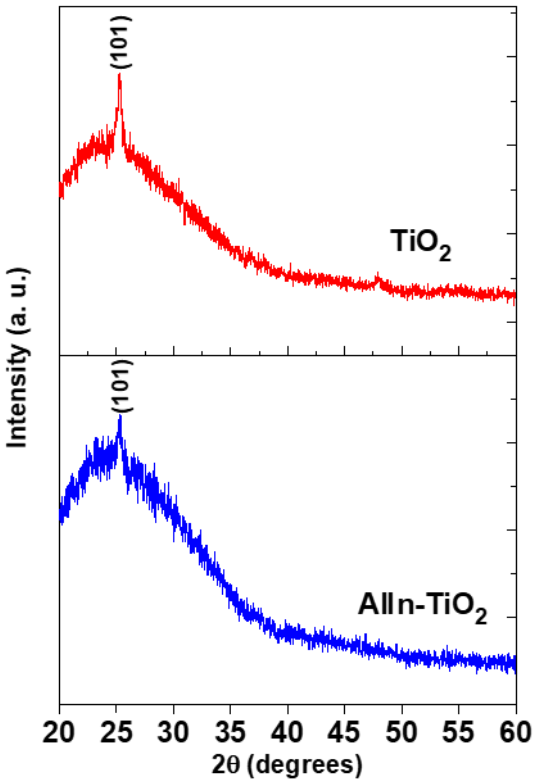

Figure S1. X-ray diffraction patterns of TiO_2 and AlIn-TiO_2 films.

From the cross sectional SEM images, there was negligible difference in thickness of both pristine TiO_2 and AlInTiO_2 films, whereby both films had similar thicknesses of 60 nm. Such low doping concentration in our doped film makes no impact on the film formation in our spin-casting technique. As such, the decrease in peak intensity is probably due to the presence of dopant in our film.

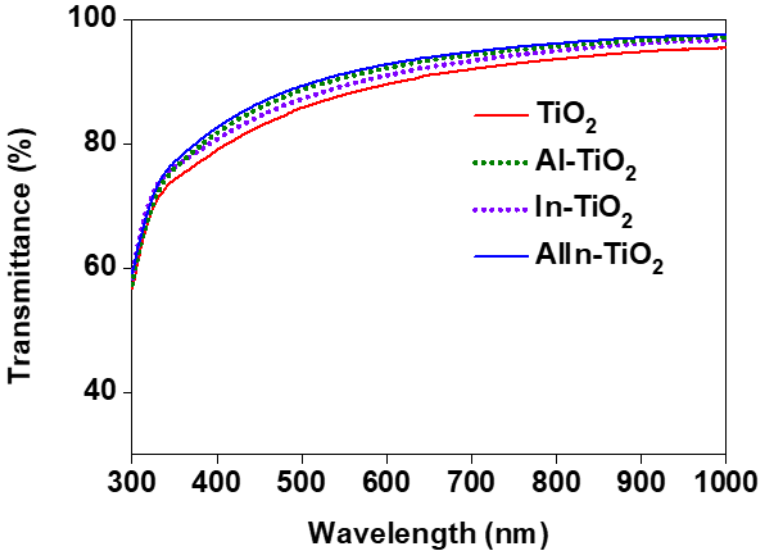

Figure S2. Transmittance spectra of TiO_2, Al- TiO_2. In- TiO_2 and AlIn-TiO_2 films.

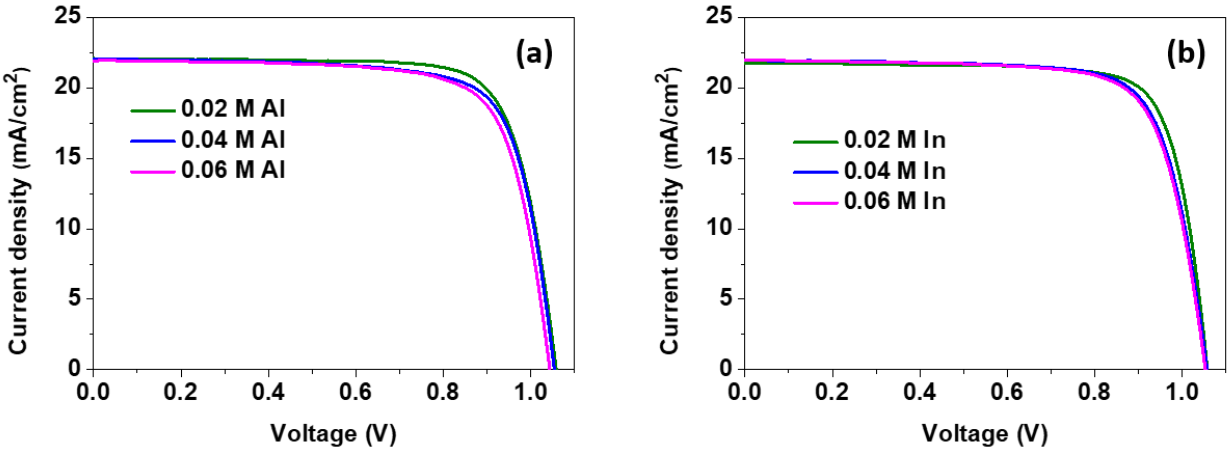

Figure S3. Current density-voltage (J-V) characteristics of perovskite solar cells with Al-TiO_2 and In-TiO_2 ETLs.

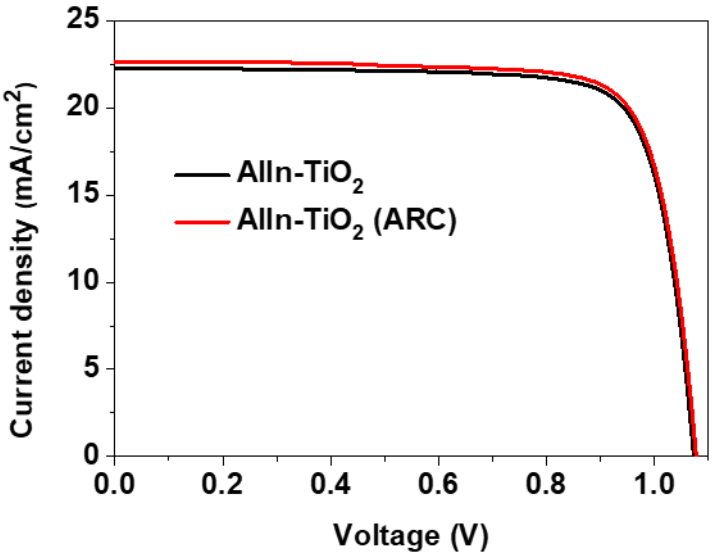

Figure S4. Current density-voltage (J-V) characteristics of AlIn-TiO_2 based perovskite solar cells with and without anti-reflection film (ARC).

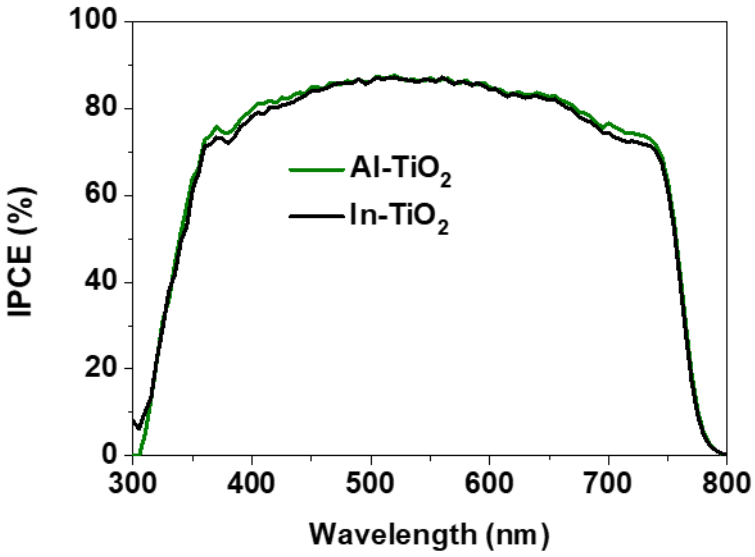

Figure S5. IPCE spectra of perovskite solar cells with Al-TiO_2 and In-TiO_2.

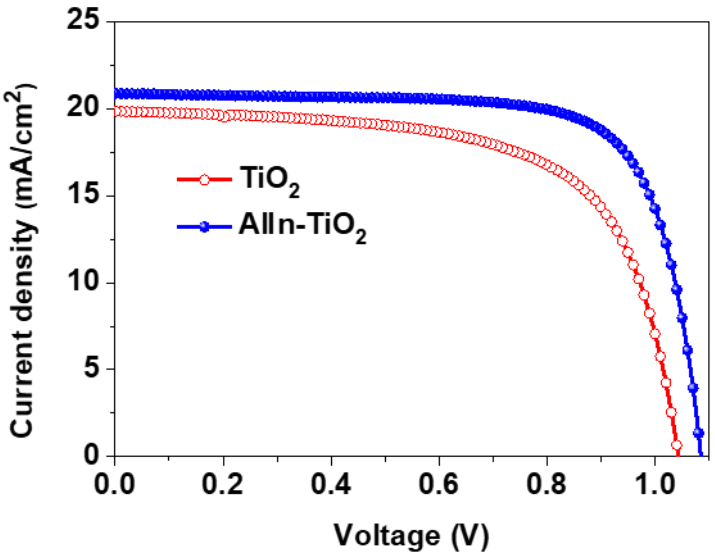

Figure S6. Current density-voltage (J-V) curves of the TiO_2 and AlIn-TiO_2 based perovskite solar cells after 25 days in ambient condition.

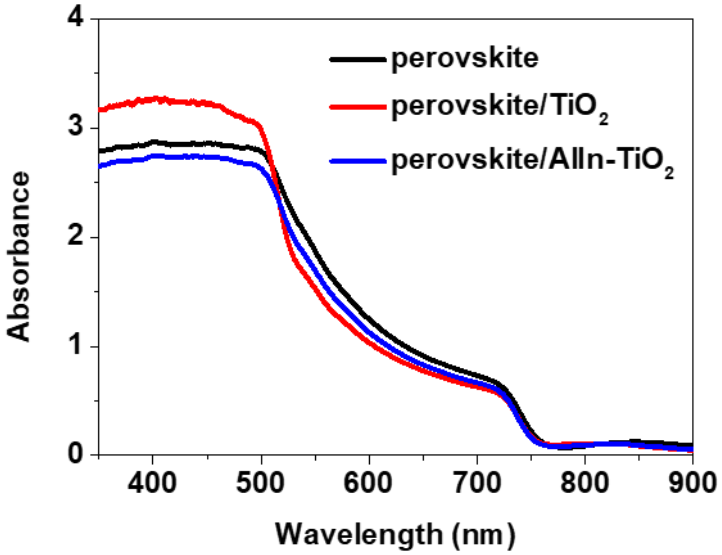

Figure S7. Absorption spectra of perovskite coated TiO_2 and AlIn-TiO_2 films.

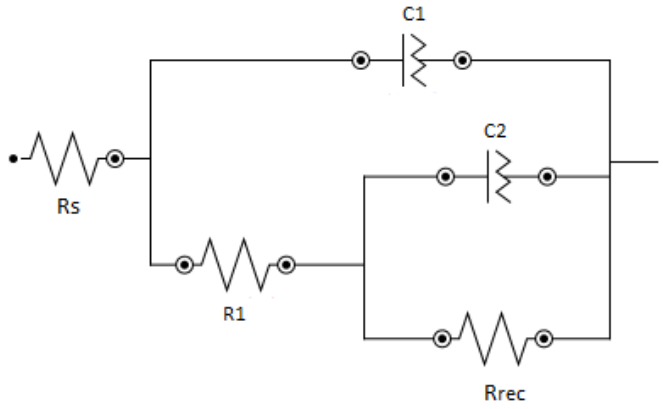

Figure S8. Equivalent circuit for the analysis of perovskite solar cells.

To gain more insight into the charge transport and recombination dynamics in the devices, EIS measurements were carried out for the TiO_2 and AlIn-TiO_2 based devices under dark in the Ar atmosphere (glove box). The impedance spectra exhibited two arcs in the complex impedance plot as reported widely in literature for devices with good charge extraction. The data was analysed using the commonly reported [1-2] equivalent circuit consisting of a series resistance (R_s), two capacitive (C_1 and C_2) and two resistive components (R_{rec} and R_1). The series resistance arises from the Ohmic contribution from wires and contacts. Capacitance C_1 related to the high frequency part of the spectra originates from the dielectric bulk capacitance of the device and the low frequency capacitance C_2 is generally associated with the trapping and detrapping of carriers. The origin of the resistances R_1 and R_{rec} are not clearly established but they are often associated with the bulk conductivity and recombination resistance of the device.

Table S1: Photovoltaic parameters of perovskite solar cells with Al-TiO_2 and In-TiO_2.

ETLs	Voc [V]	Jsc [mA cm^{-2}]	FF [%]	PCE [%]
0.04 M Al-doped TiO_2	1.05	22.04	75.26	17.43
0.06M Al-doped TiO_2	1.04	22.02	74.93	17.15
0.04 M In-doped TiO_2	1.05	21.94	75.89	17.57
0.06 M In-doped TiO_2	1.05	21.98	75.02	17.33

Table S2: The Hall effect parameters of TiO_2 and AlIn-TiO_2 devices, with structure of glass/TiO_2 (or AlIn-TiO_2)/Au.

ETLs	Type	Hall mobility ($cm\ V^{-1}S^{-1}$)	Carrier density ($1/cm^3$)	Resistivity (Ohm*cm)	Conductivity ($S\ cm^{-1}$)
TiO_2	N	1.03	2.14×10^{14}	28310	3.53×10^{-5}
AlIn-TiO_2	N	1.15	2.85×10^{14}	18926	5.28×10^{-5}

Table S3: Analysis of the TRPL with two-exponential decay characteristics for perovskite, perovskite/TiO_2 and perovskite/AlIn-TiO_2.

Samples	**A_1**	**τ_1 (ns)**	**A_2**	**τ_2 (ns)**	**$\tau_{average}$ (ns)**
Perovskite	0.25	8.47	0.75	309.1	233.9
Perovskite /TiO_2	0.20	9.10	0.80	258.4	208.5
Perovskite /AlIn- TiO_2	0.32	10.6	0.68	215.7	150.1

Table S4: The fitted parameters for EIS measurements acquired under dark condition.

ETLs	R_{series} (Ω)	R_{rec} (KΩ)
TiO_2	19.5	5.40
AlIn- TiO_2	18.7	56.9

References

[1] A. Guerrero, G. G.-Belmonte, I. M.-Sero, J. Bisquert, Y. S. Kang, T. J. Jacobsson‖, J.-P. C.-Baena, A. Hagfeldt, *J. Phys. Chem. C* **2016**, *120*, 8023.

[2] I. Zarazua, G. Han, P. P. Boix , S. Mhaisalkar, F. F.-Santiago, I. M.-Seró , J. Bisquert, G. G.-Belmonte, *J. Phys. Chem. Lett.* **2016**, *7*, 5105.